ROYAL SOCIETY
OF CHEMISTRY

PAPER

Nanocrystalline CoMnFeNiGa high entropy alloys: room temperature ferromagnetism bridging the gap from bulk to nano†

N. F. Shkodich, [ID] *[a] T. Smoliarova,[a] V. Nallathambi, [ID] [bc] L. M. Feitosa,[c] E. Adabifiroozjaei,[d] I. Tarasov,[a] M. Grzywa,[e] B. Gault, [ID] [cf] S. Reichenberger, [ID] [b] L. Molina-Luna, [ID] [d] S. Barcikowski [ID] [b] and M. Farle [ID] [a]

Nanocrystalline CoMnFeNiGa high entropy alloys (HEAs) were successfully synthesized and characterized across different length scales. Compositionally homogeneous single-phase FCC HEA micropowder particles with a nanocrystalline structure ($\sim$8 nm) were produced by short-term (190 min) high energy ball milling (HEBM). These powders were subsequently used as precursors for fabricating dense HEA bulk by spark plasma sintering (SPS) and HEA nanoparticles (NPs) by laser fragmentation in liquids (LFL)—both synthesis routes are not achievable by direct processing of elemental powder blends. We show that the single-phase FCC CoMnFeNiGa HEA micropowder partially transforms into a BCC phase upon consolidation by SPS at 1073 K. As a result, the HEA bulk consists of a mixture of FCC and BCC phases. In addition, Mn-rich BCC precipitates (10–50 nm) were formed in both HEA phases. The LFL of HEA micropowder leads to a formation of HEA NPs with two morphologies (spheres and quasi-2D platelets with 5–10 nm thickness and 40–150 nm lengths) with FCC, BCC, and hexagonal structures (birnessite-type layered δ-MnO_2 structure). All three nanocrystalline CoMnFeNiGa HEAs exhibit soft ferromagnetic behavior at RT with a saturation magnetization (M_s) of 19.5–33.5 A m^2 kg^{-1} for the micropowder and NPs, while the M_s of HEA bulk is 2–4 times larger (88.8 A m^2 kg^{-1}). A short thermal treatment (1000 K, 30 s) significantly enhanced M_s and increased the Curie temperature of the

[a]Faculty of Physics and Center of Nanointegration (CENIDE), University of Duisburg-Essen, 47057 Duisburg, Germany. E-mail: natalia.shkodich@uni-due.de

[b]Technical Chemistry I and Center for Nanointegration Duisburg-Essen (CENIDE), University of Duisburg-Essen, 45141 Essen, Germany

[c]Max Planck Institute for Sustainable Materials, Max-Planck-Str. 1, 40237 Düsseldorf, Germany

[d]Advanced Electron Microscopy Division, Institute of Materials Science, Department of Materials and Geosciences, TU Darmstadt, Peter-Grünberg-Str. 2, Darmstadt 64287, Germany

[e]Rigaku Europe SE, Hugenottenallee 167, 63263 Neu-Isenburg, Germany

[f]Department of Materials, Royal School of Mines, Imperial College London, Prince Consort Road, London SW7 2BP, UK

micropowder to 105.6 A m^2 kg^{-1} and 785 K, of the NPs to 46.9 A m^2 kg^{-1} and 850 K, and of the bulk material to 106 A m^2 kg^{-1} and 793 K. The coercivity increased threefold to 1.8 kA m^{-1} only in NPs. Structure–property relationships in CoMnFeNiGa HEAs are herein systematically compared across all length scales, demonstrating that magnetic behavior can be effectively tuned by nanoscale structural control and rapid thermal treatment.

1. Introduction

High entropy alloys (HEAs) have garnered significant attention in recent years due to their unique synergy of structural, physical, chemical, and magnetic properties, which arise from their multi-principal element design.[1–15] Typically composed of five or more principal elements in near-equiatomic ratios, HEAs exhibit significant chemical disorder that strongly influences configurational entropy (ΔS_{conf}), Gibbs free energy (ΔG), and ultimately, phase selection and stability. The atomic size mismatch (<6.5%) among constituent elements leads to lattice distortion, contributing to the overall thermodynamic stability of HEAs.[16] The ΔS_{conf} promotes the formation of simple solid solution phases – body-centered cubic (BCC),[12,16] face-centered cubic (FCC)[1,7,17] or hexagonal closest packed (HCP)[18,19] – while kinetically hindered the formation of intermetallic compounds, thereby enabling the design of materials with property combinations unattainable through conventional approaches. In addition, the vast unexplored compositional space of HEAs offers significant potential for discovering novel functional materials.[20]

Beyond their exceptional mechanical properties,[8–12] and structural stability,[7,14–21] HEAs have also attracted increasing attention for their magnetic properties. They have emerged as promising candidates for next-generation soft magnetic materials, offering the combination of high saturation magnetization (M_s) and enhanced mechanical performance and improved structural stability.[3,13] Additionally, magnetic HEAs (MagHEAs) have shown significant potential for magnetocaloric applications.[5] Furthermore, recent reports have highlighted the hard magnetic behavior in FeCoNiAlCu$_x$Ti$_x$-based HEAs.[6,22]

MagHEAs typically consist of 3d transition elements, where Fe, Co, and Ni provide strong magnetic responses due to their aligned spins. For instance, a FeCoNi alloy has a M_s at 300 K of 151.3 A m^2 kg^{-1}.[23] However, incorporating elements like Mn, introduces competing antiferromagnetic (AFM) interactions that reduce the net magnetization. As a result the FeCoNiMn alloy exhibited a M_s (300 K) of 18.8 A m^2 kg^{-1} [24] only, nearly one order of magnitude lower. Further addition of sp-type elements like Al, Sn, Ge, and Ga typically leads to the formation of a BCC structure and can significantly alter the magnetic behavior, *e.g.* an enhanced ferromagnetic (FM) order, increased Curie temperature (T_c) and improved thermal stability.[24–28] While the effects of Al addition have been widely explored in single-phase FCC CoMnFeNi alloy,[24–27] the influence of Ga on magnetic ordering remains relatively unexplored and has only been studied in bulk samples produced using conventional multistep melting routes.[24,26,28] These approaches often result in compositional inhomogeneity and require extended annealing at high temperatures followed by quenching, to achieve more uniform microstructures. Thus, grain sizes typically reach hundreds of micrometers, and composition control becomes particularly challenging during melting due to the

presence of low-melting/boiling elements like Ga (T_{melt} = 302.9 K). Alternatively, high energy ball milling (HEBM) is a simple, cost-effective, and scalable non-equilibrium synthesis route capable of producing homogeneous, nano-crystalline HEA powders by extending solubility limits and suppressing phase segregation.[20,30] In our recent work,[17] we showed that HEBM can be successfully used to homogeneously incorporate low melting Ga atoms into the HEA structure while preserving the initial elemental concentration ratios. For further commi-nution into nanoparticles (NPs), pulsed laser fragmentation in liquids (LFL) ideally complements with HEBM and can yield surfactant-free kinetically stabi-lized colloidal nanoparticles as a down-stream powder processing technique.[31–34]

Conceptually, the complexity of the magnetic response within the HEAs arises from locally varying exchange coupling between the elements. These interactions are influenced by the sintering route yielding different morphology and micro-structure of the material—either in bulk, powder, or nanoparticle form. Changing and controlling nanocrystallinity and microstructures across different length scales offers an interesting pathway to design HEAs with enhanced functional properties adapted to special applications.

Here, we demonstrate how different processing approaches and short thermal treatment influence the structural evolution and magnetic properties of CoMn-FeNiGa HEA across different length scales. First, short-term single step HEBM was successfully used for the synthesis of homogeneous nanocrystalline single-FCC HEA powder from elemental powders and Ga ingots. Second, to obtain the HEA bulk, the HEA powders were then consolidated by spark plasma sintering (SPS), which allows the rapid consolidation of powders at relatively low temper-atures and short processing times and helps to prevent significant grain growth, while maintaining the desired nanocrystalline structure.[18,29,35] To extend the investigation to the nanoscale, microparticle laser fragmentation in liquids (MP-LFL)[32,33] was applied to generate HEA NPs, enabling the study of size- and morphology-dependent magnetic phenomena under rapid quenching condi-tions. This combined processing strategy provides unique insight into the structure–property relationships in HEAs and highlights the tunability of magnetic behavior through tailored synthesis routes.

2. Experimental

The CoMnFeNiGa HEA micropowders were prepared by HEBM of elemental powders: Co (99.5%, 45–60 μm), Mn (99.5%, 325 mesh), Fe (99.96%, 10–20 μm), Ni (99.5%, 45–60 μm), and Ga ingots (99.99%) taken in equiatomic concentrations.

HEBM was performed in a water-cooled planetary ball mill "Activator-2S" using stainless-steel vials and balls (Ø = 7 mm) as illustrated in Fig. 1a. In all cases the ball-to-powder weight ratio was 20 : 1. The vial was evacuated and then filled with Ar gas at 4 bars to prevent oxidation during the process. The HEBM was carried out at a rotation speed of the sun wheel/jars: 900 rpm/1800 rpm. Milling time (t) in Ar ("dry" conditions) varied from 30 to 180 min. An additional milling for 10 minutes in C_3H_7OH was applied.

For the synthesis of CoMnFeNiGa HEA bulk, the single-phase FCC HEA (HEBM t = 190 min) micropowder was consolidated by SPS in vacuum in a Labox 650 facility (Sinter Land, Japan). The HEA powder was placed into a cylindrical
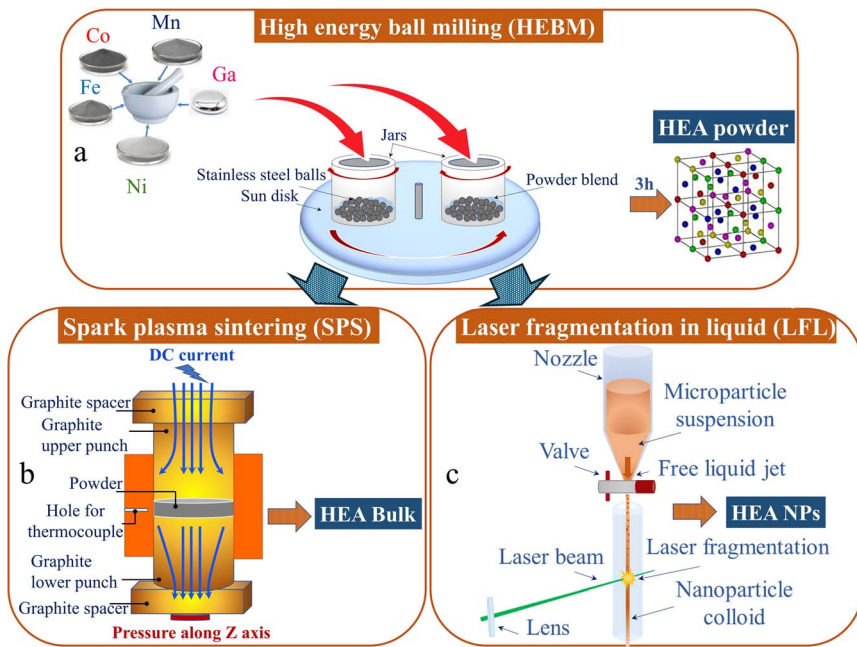
Fig. 1 A schematic diagram of (a) high energy ball milling (HEBM), (b) spark plasma sintering (SPS), and (c) Laser fragmentation in liquids (LFL) processes for the synthesis of nanocrystalline HEA micropowders, HEA bulk, and HEA nanoparticles, respectively.

graphite die (inner diameter 12.7 mm) and uniaxially compressed at 10 MPa. The sample was heated at a rate of 100 K min^{-1} up to 1073 K by passing rectangular pulses of electric current through it. The dwell time at the sintering temperature was 10 min. SPS-produced disks were 2–3 mm thick and 12.7 mm in diameter (see Fig. 1b).

The microparticle fragmentation experiments for nanoparticles synthesis were carried out using a nanosecond pulsed laser (IS160-1-T, EdgeWave GmbH) with a wavelength of 532 nm, pulse duration of 7 ns, repetition rate of 5 kHz and pulse energy of 15 mJ. The microparticles were dispersed in Milli-Q water at a concentration of 1 g L^{-1} and ultrasonicated for 30 min to get a uniform dispersion. A cylindrical flow jet (Fig. 1c) of the microparticle dispersion was then irradiated multiple times using the pulsed laser in the direction perpendicular to the liquid flow as detailed in ref. 34. The colloidal dispersion after fragmentation was allowed to rest for 1 h before removing the remaining sedimented microparticles. The pH of the nanoparticle colloid was then adjusted to pH 6.5 to maintain long-term stability.

Crystal structures of the samples were characterized by X-ray diffraction (Panalytical X'pert Pro diffractometer with Fe K$_\alpha$ and Cu K$_\alpha$ radiation, $2\theta = 10$–$120°$). To determine the phases, lattice parameters, crystallite size and microstrains, the refinements of the XRD data were performed using Maud software.[36] Variable-temperature X-ray powder diffraction (VT-XRPD) measurements were conducted using a Rigaku SmartLab XE diffractometer equipped with a PhotonMax Cu rotating anode source (9 kW, 45 kV, 200 mA) and a two-dimensional

XSPA-400 ER detector. Data acquisition was performed in reflection geometry over the 2θ range of 40–85°, with a step size of 0.04° and a scan rate of 50° min^{-1}. Temperature-dependent measurements were carried out using an Anton Paar HTK 1200N high-temperature oven chamber. The sample was heated from ambient temperature to 1000 K at a rate of 10 K min^{-1}, followed by cooling to room temperature (RT). Diffraction patterns were continuously recorded throughout the heating and cooling cycles, with each scan collected over a duration of 1.5 minutes. Measurements were conducted under a nitrogen atmosphere with a controlled flow rate of 150 mL min^{-1}. Data acquisition commenced two hours after the sample was placed in the heating chamber and nitrogen flow was initiated.

Scanning electron microscopy (SEM; Thermo Scientific Phenom Pharos G2 FEG-SEM and Zeiss LEO 1530) in secondary electron (SE) and backscattered electron (BSE) modes equipped with energy dispersive X-ray spectroscopy (EDX, Oxford Instruments XMAX, 80 mm^2) were used for microstructural and compositional analysis.

Transmission electron microscopy (TEM) studies of HEBM micropowder and LFL NPs were performed using a Jeol 2200FS cs-aberration corrected TEM at an acceleration voltage of 200 kV using a 2k × 2k GATAN UltraScan 1000XP CCD camera. The elemental distribution was analyzed in scanning (S) TEM mode with a windowless 80 mm^2 SDD X-MaxN TLE energy-dispersive X-ray spectroscopy (EDXS) detector (Oxford Instruments). TEM specimens were prepared by dropping the well-dispersed HEA micropowder and NPs water solutions (∼3 µL) onto a C-coated Cu grid and letting the grid air-dry before inserting into microscope. TEM lamella of the SPS bulk sample was prepared with a precision ion-polishing system (PIPS, Gatan Dual Ion Mill Model 600). High-angle annular dark-field (HAADF) imaging was subsequently performed on a JEOL ARM200F operated at an accelerating voltage of 200 kV. For the *in situ* heating study, ∼3 µL of LFL NPs dispersion were deposited onto a Lightning Nano-Chip (DENSsolutions B.V.), dried at 60 °C for 24 h, and then mounted in a DENSsolutions Lightning HB+ (former D9+) *in situ* TEM holder. The NPs were heated for 30 min at successive temperatures ranging from room temperature up to 1273 K.

The 3D nanoscale elemental distribution in the SPS-consolidated HEA was investigated by atom probe tomography (APT) (LEAP 5000X HR, Camera Inc.) at a pulse repetition rate of 200 kHz in voltage pulsing mode (15% of pulse frequency). The base specimen temperature was maintained at 50 K and the target detection rate was set to five ions detected every 1000 pulses. The site-specific lift-out for APT specimen preparation was performed from HEA bulk with a focused ion beam (FIB) instrument (FIB Helios Nanolab 600i).[37] The data analysis was done using the software APSuite 6.3.

Magnetic properties of the HEA micropowders, HEA bulk, and HEA NPs were determined using a Quantum Design Dyna Cool Physical Property Measurement System (PPMS) at various temperatures (5–1000 K) under external magnetic fields of up to 9 tesla. The error bar of: (a) M does not exceed 0.05%; (b) T_c is ± 2 K; (c) H_c is ± 0.5%. The M_s values were taken after extracting the slope in each field-dependent magnetization $M(H)$ curve. The slope at high fields can be attributed to paramagnetic or field-dependent alignment of non-collinear magnetic moments in the sample.

3. Results

3.1 Structure and composition of CoMnFeNiGa HEAs at different length scales

3.1.1 CoMnFeNiGa HEA micropowder. Fig. 2a represents a set of XRD patterns of the CoMnFeNiGa powder mixtures milled for different HEBM times (t). The non-milled powder blend exhibits sharp Bragg peaks corresponding to the constituent elements—Co, Mn, Fe, and Ni—excluding Ga (X-ray amorphous at RT) (Fig. 2a, black). Due to close atomic sizes, the diffraction peaks of the Fe (110), Ni (111) and Co (002), as well as Co (102) & Fe (200); and Co (110) & Ni (220) are partially overlapped (Fig. 2a, black). The HEBM carried out over a period of 0–190 minutes, induces significant structural transformations in the initial powder blend. After HEBM $t = 15$ min all these peaks fused together forming broader ones. At HEBM $t = 30$ min, the diffraction peaks of the individual elements vanish completely, indicating their dissolution to the matrix followed by a formation of two solid solutions with BCC and FCC structures. Further milling (up to 120 min) leads to a gradual BCC → FCC structural transformation (Fig. 2a, HEBM t indicated to the left). After HEBM $t = 120$ min, this transformation results in the formation of a single-phase FCC structure composed of multiple elements.

Further milling ($t = 120$–190 min) does not notably change the XRD spectrum of the alloy. The lattice parameters, crystallite size, and microstrain of single-phase FCC CoMnFeNiGa solid solutions, formed after 180 min ("dry" conditions: Ar) and 190 min ("dry + wet" conditions: 180 min (Ar) + 10 min (C_3H_7OH)) of HEBM, were determined by Rietveld refinement (see details in S1 of the ESI†). The results of the calculations are summarized in Table 1.

Both "dry" and "dry + wet" milled CoMnFeNiGa HEA powders exhibit a single-phase FCC crystal structure with a slight tetragonal distortion (see Table 1). For the "dry" milled sample, the lattice parameters yield a distortion of approximately 1%. An additional short-wet milling step (10 min in C_3H_7OH) results in a slight reduction of the in-plane lattice parameters (a and b), while the c parameter remains nearly unchanged, leading to a slightly increased tetragonal distortion of
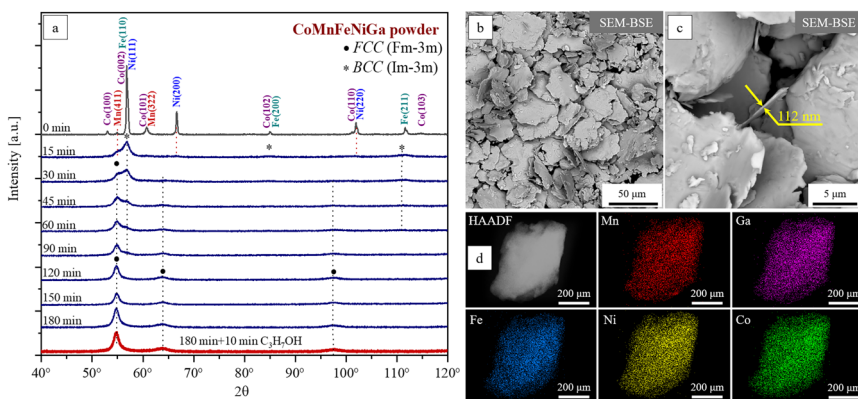

Fig. 2 (a) XRD patterns of CoMnFeNiGa powder mixtures taken after HEBM for different t (indicated at the left); (b) and (c) SEM images with different magnifications; (d) STEM image with EDX mapping of elements of CoMnFeNiGa microparticle produced by HEBM for 180 min in Ar and additional HEBM for 10 min in C_3H_7OH at 900/1800 rpm.

Table 1 Crystal structure parameters for CoMnFeNiGa HEA powders synthesized in "dry" (180 min (Ar)) and "dry + wet" (180 min (Ar) + 10 min (C₃H₇OH)) HEBM conditions

Sample	Structure	a, b, c [nm]	Crystallite size [nm]	Microstrain [%]
CoMnFeNiGa powder; HEBM: 180 min (Ar)	FCC	$a = b = 0.3667 \pm 0.0004$ $c = 0.3703 \pm 0.0001$ Tetragonal distortion $\sim 1\%$	10 ± 0.4	0.6 ± 0.1
CoMnFeNiGa powder; HEBM: 180 min (Ar) + 10 min (C₃H₇OH)	FCC	$a = b = 0.3656 \pm 0.0002$ $c = 0.3701 \pm 0.0002$ Tetragonal distortion $\sim 1.2\%$	8 ± 0.2	0.4 ± 0.1

$\sim 1.2\%$. It also causes an $\sim 20\%$ reduction in crystallite size (to 8 ± 0.2 nm) and a decrease in microstrain from $0.6 \pm 0.1\%$ to $0.4 \pm 0.1\%$, indicating that the presence of isopropanol facilitates strain relaxation during milling. Overall, the short wet-milling step produces a finer, less strained microstructure with slightly enhanced anisotropy.

By varying the HEBM conditions ("dry" and "dry + wet") the morphology of the single-phase FCC HEA powders can be tailored. The powders synthesized under "dry" HEBM conditions exhibit a rounded shape morphology with particle sizes ranging from 5 to 100 μm. In contrast, the addition of a short wet-milling step induces a transition to a flake-type morphology characterized by similar lateral dimensions (~ 5–100 μm) but significantly reduced thicknesses on the order of 100–500 nm (Fig. 2b and c).

SEM-EDX analyses performed on both the surface and cross-section of the HEA powders show better compositional homogeneity at the microscale for the flake-type powders, which retain the nominal near-equiatomic composition (at%): Co 19.8 ± 0.5, Mn 20.1 ± 0.4, Fe 19.8 ± 0.5, Ni 20.0 ± 0.4, and Ga 20.3 ± 0.3 (see details in S2 of the ESI†). STEM-EDX analysis (Fig. 2d) further confirms a homogeneous distribution of the principal elements within the flake-type HEA particles, as well as the retention of their nominal equiatomic concentrations (at%: Co 21.2 ± 0.6; Mn 19.8 ± 0.3; Fe 21.2 ± 0.5, Ni 18.7 ± 0.6, and Ga 19.0 ± 0.5) at the nanoscale.

Accordingly, the flake-type CoMnFeNiGa HEA micropowder was selected as the precursor material for the subsequent synthesis of HEA NPs, fabrication of HEA bulk, and the detailed magnetic characterization.

3.1.2 CoMnFeNiGa HEA nanoparticles. In contrast to the single-phase FCC HEA micropowder synthesized by HEBM, the XRD pattern of the NPs after LFL exhibits a complex multiphase composition, primarily dominated by a hexagonal birnessite-type layered δ-MnO₂ structure (72 ± 10 vol%). It shows orthorhombic symmetry with lattice parameters $a = 0.5425 \pm 0.0006$ nm, $b = 0.2820 \pm 0.0005$ nm, and $c = 0.7744 \pm 0.0005$ nm. The average 2D crystallite thickness is about 0.8 nm. Solid solution BCC and FCC phases contribute approximately 19 ± 10.1 vol% and 6.5 ± 0.1 vol%, respectively. Additionally, a minor fraction (2.5 ± 0.1 vol%) of goethite (FeO(OH)) is also present (Fig. 3a, red). This suggests that the metal–liquid interactions and oxidizing conditions during laser fragmentation in water promote phase segregation and structural transformation.[38] The observed layered hexagonal structures notably resemble Fe–Ni mixed metal nanosheets
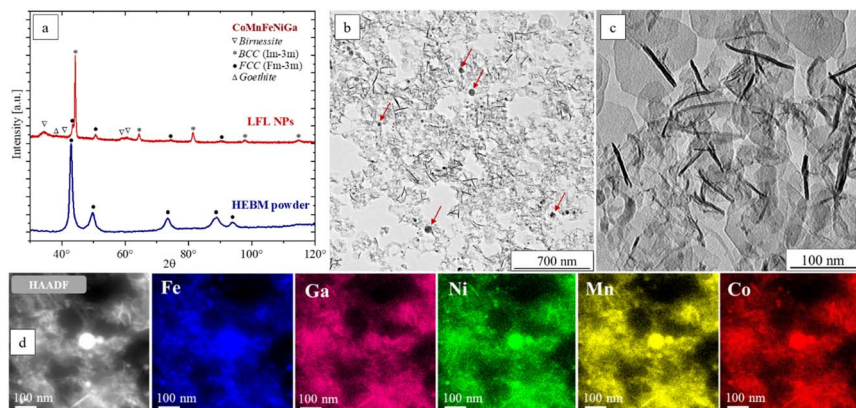
Fig. 3 (a) XRD patterns of CoMnFeNiGa HEA NPs after LFL (red) and HEA powder (blue); bright-field TEM images displaying two distinct morphologies: (b) spheres (red arrows) and (c) hexagonal nanoplates; (d) high-angle annular dark-field STEM image with the corresponding EDX elemental maps of Fe (16.2 ± 0.6 at%), Mn (37.5 ± 0.8 at%), Co (14.3 ± 0.8 at %), Ni (12.4 ± 0.6 at%), and Ga (19.6 ± 0.3 at%).

previously produced through laser synthesis techniques.[39] The lattice parameters of the FCC phase in the NPs are ($a = b = c = 0.3601 \pm 0.0002$ nm) approximately 1.5% smaller compared to those in the micropowder (Table 1). The crystallite size is 6 times larger (49 ± 2.4 nm), while the microstrain value (0.24 ± 0.06%) is doubled reduced compared to the micropowder (Table 1). The minor fraction of the FCC phase which remained after LFL synthesis is found to be structurally more uniform and less strained.

TEM analysis of the NPs reveals two distinct morphologies: spheres and hexagonal platelets. The spherical NPs exhibit diameters of 5–30 nm (Fig. 3b, red arrows), whereas the platelets have lateral dimensions of ∼40–150 nm and an apparent thickness of 5–10 nm, estimated from the dark needle-like stripes corresponding to platelets oriented perpendicular to the electron beam (Fig. 3c).

The elemental EDX mapping was performed on an area combining both NPs morphologies, presented by the high-angle annular dark-field (HAADF) STEM image (Fig. 3d) accompanied with the corresponding elemental maps confirming a homogeneous distribution of Fe (16.2 ± 0.6 at%), Mn (37.5 ± 0.8 at%), Co (14.3 ± 0.8 at%), Ni (12.4 ± 0.6 at%), and Ga (19.6 ± 0.3 at%) throughout the particles of different morphologies. An oxygen signal is also detected, which correlates with the XRD detection of birnessite-type layered δ-MnO_2 and goethite ($FeO(OH)$) structures known to be hydroxide or oxyhydroxide compounds.

The quasi-2D morphology of the hexagonal platelets was further studied by three-dimensional (3D) electron tomography. Fig. 4a displays a bright-field (BF) tilt series of a representative platelet at −30°, 0°, +30°, and +60°. At −30° the platelet is almost edge-on, so it appears as a dark needle-like stripe (as shown in Fig. 3c), whereas at +60° it is nearly face-on, revealing its full hexagonal outline (Fig. 4d). This contrast between edge-on and face-on images confirms that the thickness of the platelet is much smaller than its lateral dimensions. Fig. 4e represents the HAADF-STEM image of a typical face-on single platelet, from which the EDX elemental maps were recorded (Fig. 4h). Due to the platelet being only ∼5
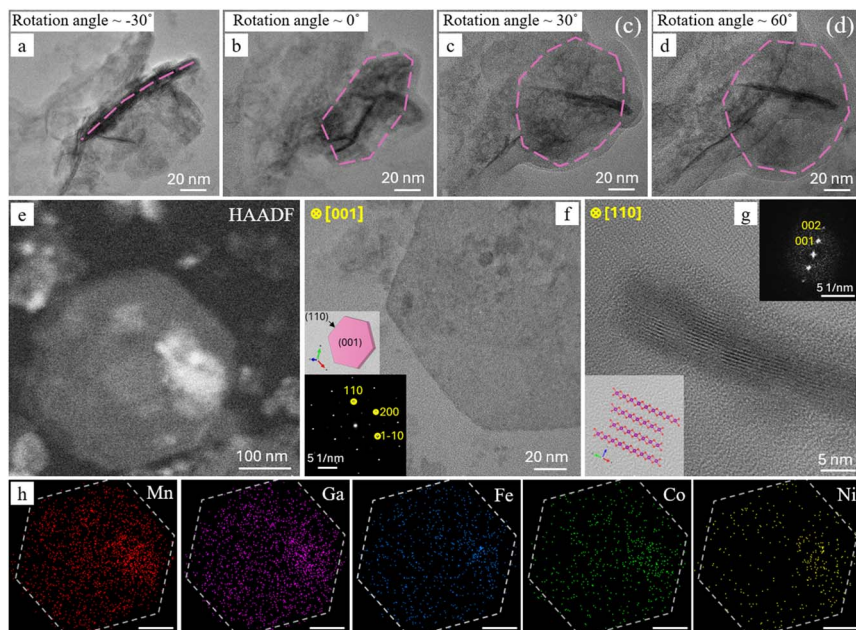
Fig. 4 Bright-field projections of a CoMnFeNiGa hexagonal platelet acquired at (a) −30°, (b) 0°, (c) +30° and (d) +60°, the platelet is highlighted with a pink dashed outline, showing variations in projected shape as the tilt angle changes from (a) edge-on to (d) face-on projection; (e) HAADF STEM image of a face-on single platelet, accompanied with (h) the EDX elemental maps of Fe (9.8 ± 0.6 at%), Mn (39.9 ± 0.5 at%), Co (9.0 ± 0.7 at%), Ni (6.1 ± 0.6 at%), and Ga (35.2 ± 0.7 at%); (f) bright-field TEM image of face-on platelet projection with SAED pattern (lower left inset) revealing the birnessite-type layered δ-MnO$_2$ structure with the [001] zone axis, and the bright inset with the crystal shape displaying the (001) face-on plane and the (110) edge-on plane, presented by (g) in bright-field HRTEM image revealing the parallel layers defining its two-dimensional structure; lower left inset displays the [110] projection of the δ-MnO$_2$ unit cell corresponding to the layered motif observed in the image, and the upper right inset presents the FFT pattern taken from this image.

nm-thick, well below the characteristic X-ray generation depth,[40] the electron–sample interaction volume is limited, producing intrinsically low count rates in the EDX elemental maps. Nevertheless, the spectra integrated over the entire platelet give the average compositions of Fe (9.8 ± 0.6 at%), Mn (39.9 ± 0.5 at%), Co (9.0 ± 0.7 at%), Ni (6.1 ± 0.6 at%), and Ga (35.2 ± 0.7 at%), which are comparable with the concentrations measured over a larger area (Fig. 3d). The structure of the platelets was studied by selected area electron diffraction (SAED), which pattern ([001] zone axis) from a single platelet is shown in Fig. 4f in the lower left inset. The pattern exhibits a sharp, six-fold array of reflections that index to the hexagonal birnessite-type layered δ-MnO$_2$ structure (space group $R\bar{3}m$, $a = b = 0.2996$ nm, $c = 1.4105$ nm, $\alpha = \beta = 90°$, $\gamma = 120°$). The face-on projection corresponds to the (001) plane and the edge-on to the (110), as shown in the inset with the crystal shape. Fig. 4g presents an edge-on BF-HRTEM image of a representative HEA platelet, clearly revealing the parallel MnO$_6$ type-structure layers that define its 2D birnessite-type architecture, also represented by the [110] projection of the δ-MnO$_2$ unit cell in the lower left inset, and FFT pattern in the upper right inset.
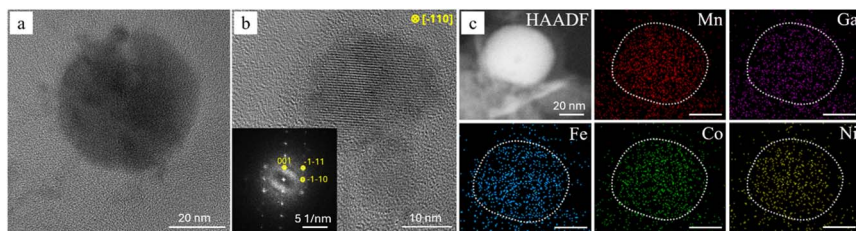
Fig. 5 (a) Bright-field TEM image of a CoMnFeNiGa sphere; (b) HRTEM image of a smaller CoMnFeNiGa sphere; the inset shows the FFT pattern indexed to the goethite FeO(OH) structure; (c) HAADF STEM image with corresponding EDX elemental maps of Fe (14.1 at%), Mn (38.8 at%), Co (15.7 at%), Ni (11.5 at%), and Ga (19.9 at%) yielding a high-entropy composition.

The morphology and structure of the spherical NPs were also studied by TEM. The BF image (Fig. 5a) shows a typical spherical NP formed after LFL. The FFT pattern taken from the HRTEM image (Fig. 5b, inset) exhibits a four-fold array of reflections that index to the cubic bixbyite-type β-Mn_2O_3 structure (space group $Ia\bar{3}$, $a = b = c = 9.769$ Å, $\alpha = \beta = \gamma = 90°$). Fig. 5c displays the HAADF-STEM image of a sphere, from which the EDX elemental maps were obtained for Fe (14.1 at%), Mn (38.8 at%), Co (15.7 at%), Ni (11.5 at%), and Ga (19.9 at%).

3.1.3 CoMnFeNiGa HEA bulk. Single-phase FCC CoMnFeNiGa HEA powders were consolidated into bulk by SPS at 1073 K (10 min) and 10 MPa. Fig. 6a represents the XRD patterns of the SPS-consolidated CoMnFeNiGa HEA (red) alongside the HEBM HEA micropowder (blue) for comparison. SPS processing
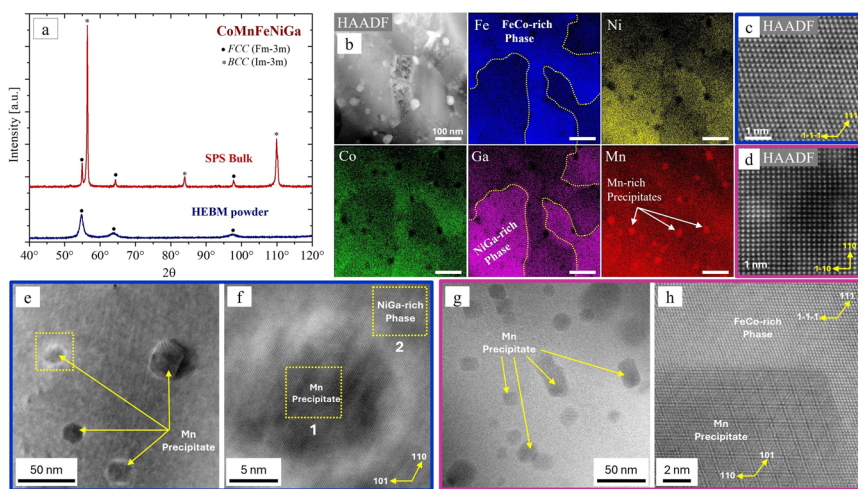

Fig. 6 (a) XRD patterns of CoMnFeNiGa HEA powder (blue) and SPS-consolidated HEA bulk (red); (b) STEM image with EDX mapping of elements of HEA bulk; (c) high-resolution HAADF image and FFT data of FeCo-rich matrix with Mn precipitates, (d) high-resolution HAADF image and FFT data of NiGa-rich matrix with Mn precipitates, (e) low- and (f) high-resolution HAADF images with different magnifications of Mn precipitates in FeCo-rich matrix, (g) low- and (h) high-resolution HAADF images with different magnifications of Mn precipitates in NiGa-rich matrix.
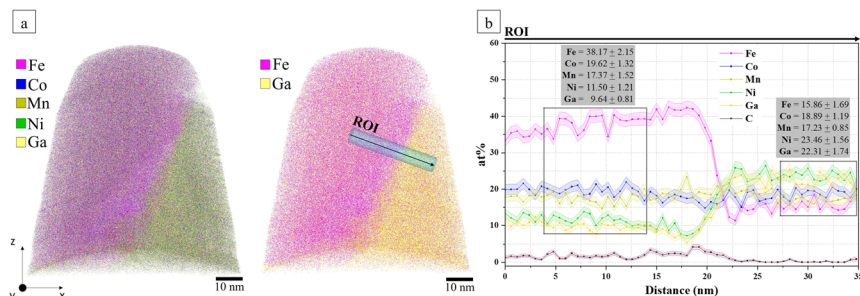
Fig. 7 APT of CoMnFeNiGa HEA bulk: (a) on the left: reconstruction showing the distribution of the main ions Fe, Co, Mn, Ni, and Ga; on the right: reconstruction depicting only Fe (pink) and Ga (yellow) distribution, with a region of interest (ROI) selected in between the two different composition areas; (b) composition distribution in the ROI with the average composition calculated from the selected points in the squares.

leads to: (a) a partial FCC → BCC phase transformation, with the FCC/BCC phase volume ratio estimated at 13%/87%; (b) an increase in the crystallite size of the FCC phase by a factor of approximately 14; and (c) a reduction in microstrain to ~0.07% (see details in S5 of the ESI†).

The cross-sectional SEM-EDX analysis revealed a uniform equiatomic distribution of the principal elements at the microscale (see details in S5 of the ESI†). However, to distinguish the chemical compositions of the FCC and BCC phases identified by XRD (Fig. 6a, red), STEM-EDX elemental maps (Fig. 6b) were recorded. They show a slight composition deviation from stoichiometry at the nanoscale. Two compositionally distinct regions can be observed: an FeCo-rich phase (at%: Fe 29.2 ± 0.5, Ni 20.2 ± 0.5, Co 24.1 ± 0.27, Ga 8.2 ± 0.5 and Mn 18.2 ± 0.2) and a NiGa-rich phase (at%: Fe 10.3 ± 0.5; Ni 32.4 ± 0.8; Co 18.2 ± 0.5, Ga 19.7 ± 0.6 and Mn 19.2 ± 0.4). Additionally, nanosized (10–50 nm) Mn-rich precipitates (at%: Mn 89.5 ± 0.4; Fe 3.4 ± 0.5; Ni 2.9 ± 0.6; Co 2.4 ± 0.2; Ga 6.6 ± 0.7) were detected in both phases.

HAADF imaging and corresponding FFT analysis of the NiGa-rich phase show that it crystallizes in BCC structure with lattice parameters $a = b = c = 0.296 \pm 0.002$ nm (Fig. 6d). Slight ordering also occurs in this phase, that could be related to the allocation of a specific site (center of the cube) to Ga. In contrast, as shown in Fig. 6c, the FeCo-rich phase corresponds to the FCC structure ($a = b = c = 0.370 \pm 0.002$ nm). There is no ordering detected. Similar HAADF analysis of the Mn-rich precipitates shows that it is crystallized in BCC structure. However, only within the FeCo-rich phase, they exhibit a characteristic five-fold modulation along the [110] reflections. The origin of this modulation remains unclear. It may be attributed to local compositional inhomogeneities or element-specific ordering effects, although its precise origin remains to be clarified.

Fig. 7 depicts the APT reconstruction of the SPS-consolidated HEA. In Fig. 7a (left), the spatial distribution of the main elements: Fe (pink), Co (blue), Mn (dark yellow), Ni (green), and Ga (yellow), is shown. The right panel of Fig. 7a shows the same dataset revealing two distinct compositional regions—one enriched in Fe (pink) and the other in Ga (yellow). A blue cylindrical region of interest (ROI) is positioned across this interface and the corresponding composition profile

calculated along the ROI is plotted in Fig. 7b. The Co partitions to the Fe-rich region, while Ni partitions to the Ga-rich region.

These APT results agree with the STEM-EDX findings (Fig. 6b). Additionally, a slightly higher concentration of carbon is detected in the Fe-rich region (Fig. 7b). This is attributed to the FCC structure of the Fe-rich phase, which is more accommodating to interstitial elements such as carbon compared to the Ga-rich BCC phase, since the octahedral interstitial sites in FCC structure support larger atomic radius than octahedral interstitial sites in BCC structure.

3.2   Magnetic properties of CoMnFeNiGa HEAs

3.2.1   CoMnFeNiGa HEA powder. The magnetic properties of CoMnFeNiGa HEA powder were investigated *in situ* as a function of temperature ($5 K \geq T \geq 1000$ K) and applied magnetic field ($-9 T \geq B_{ext} \geq 9 T$).

The temperature-dependent magnetization $M(T)$ measurements in a $B_{ext} = 1$ T are plotted in Fig. 8a. The initial $M (5 K) = 43.3$ A m^2 kg^{-1} gradually decreases to $M (450 K) = 4.1$ A m^2 kg^{-1} during the first field warming (FW^1) in the T range of 5–450 K. Then, it remains nearly constant between 450 K and 556 K, before increasing sharply at about 557 K, reaching a maximum $M = 58.9$ A m^2 kg^{-1} at 670 K followed by a continuous decrease to 0 at about 970 K, which can be attributed to a loss of ferro- or ferrimagnetic order. The first field cooling (FC^1) magnetization (Fig. 8a, blue) shows irreversible behavior beginning to increase from 950 K and reaching a value of 104.1 A m^2 kg^{-1} at 310 K, nearly 8 times higher than the initial state ($M (310 K) = 12.7$ A m^2 kg^{-1}). The second FW$^2 \rightarrow$ FC^2 (310–1000 K) cycle (Fig. 8a, red) displays an equilibrium magnetic response indicating that the material has reached a thermodynamically stable magnetic configuration. We associate this drastic change (non-monotonic) behavior of M observed during the first FW$^1 \rightarrow$ FC^1 cycle to a structural FCC $\rightarrow$ BCC phase transformation, consistent with the phase composition observed in the SPS-consolidated HEA (Fig. 6a). The magnetic transition temperature $T_1 = 240$ K of the FCC phase (before heat treatment) increases to $T_2 = 785$ K (corresponding to the BCC phase) (see details in S6 of the ESI†).
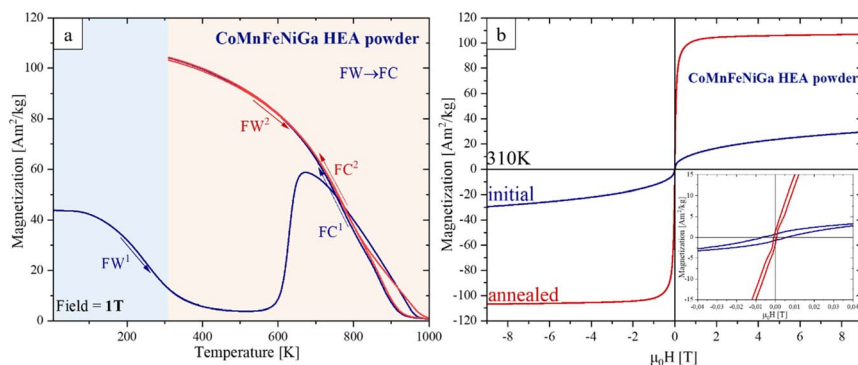

Fig. 8 CoMnFeNiGa HEA micropowder: (a) temperature-dependent magnetization $M(T)$ recorded at 1 T, (b) field-dependent magnetization $M(H)$ measured at 310 K before and after annealing ($-9 T \geq B_{ext} \geq 9 T$).

The field-dependent magnetization $M(H)$ of the CoMnFeNiGa HEA powder measured at 310 K, before and after heat treatment up to 1000 K, is shown in Fig. 8b. The heat treatment significantly enhanced the saturation magnetization M_s at 310 K (19.5 A m^2 kg^{-1})—by nearly 5 times—reaching 105.6 A m^2 kg^{-1}. At the same time, the coercivity H_c decreased from 5.1 ± 0.1 kA m^{-1} to 0.6 ± 0.1 kA m^{-1}. These results support our assumption that thermal annealing of the single-phase FCC HEA powder induces structural and/or chemical changes that favor the formation of a FM phase.

To better understand the origin of these strong magnetic changes, temperature-dependent *in situ* XRD measurements were carried out (Fig. 9). Fig. 9a shows temperature-dependent *in situ* XRD patterns in a waterfall plot, between 310 K and 750 K over a $2\theta = 40–85°$, highlighting a clear FCC → BCC phase transformation with increasing temperature. This transformation is further detailed in the 2D plot of XRD patterns in the $2\theta = 41–52°$ (Fig. 9b). The emergence of the (110) BCC peak can be observed around 569–584 K (Fig. 9b, red) followed by a gradual disappearance of the (111) and (200) FCC peaks. The FCC → BCC phase transition occurs within the temperature range of 569–724 K.

3.2.2 CoMnFeNiGa HEA nanoparticles. The temperature- and field-dependent magnetization measurements of the CoMnFeNiGa HEA NPs (mixture of spheres and 2D hexagonal platelets) were conducted under the same conditions as for the HEA micropowder. As shown in Fig. 10a, the $M(T)$ curve during the FW^1 cycle ($T = 5–1000$ K) shows a complex non-monotonic behaviour with several inflection points at approximately 150 K; 290 K; 600 K; 667 K; 767 K. The initial M (5 K) = 31.4 A m^2 kg^{-1} decreases by ~15% upon heating to 150 K followed by a recovery of similar magnitude upon reaching 290 K. Then it linearly decreases to 600 K (where a subtle inflection point is observed) reaching the value of 22.3 A m^2 kg^{-1}. A slight increase in M (second rounded maxima) was observed around 670 K, followed by a drop to almost zero at 1000 K. During the FC^1 the M increases in temperature starting from 1000 K, reaching a value of 46.2 A m^2 kg^{-1} at 310 K, which corresponds to the double increase compared to the initial state. The subsequent FW^2–FC^2 cycle (310–1000 K) exhibits a reversible and stable magnetic response from HEA NPs with the $T_c = 850$ K (see details in S6 of the ESI†).
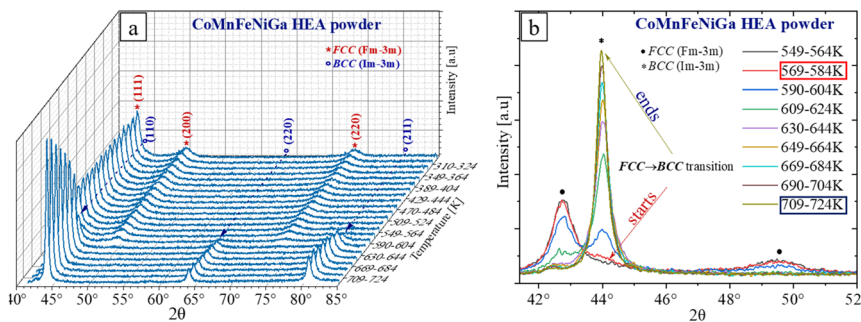

Fig. 9 Temperature-dependent *in situ* XRD patterns of CoMnFeNiGa HEA: (a) waterfall plot for $T = 310–750$ K and $2\theta = 40–85°$; (b) XRD patterns between 549 K and 724 K revealing the changes of Bragg peaks from FCC to BCC.
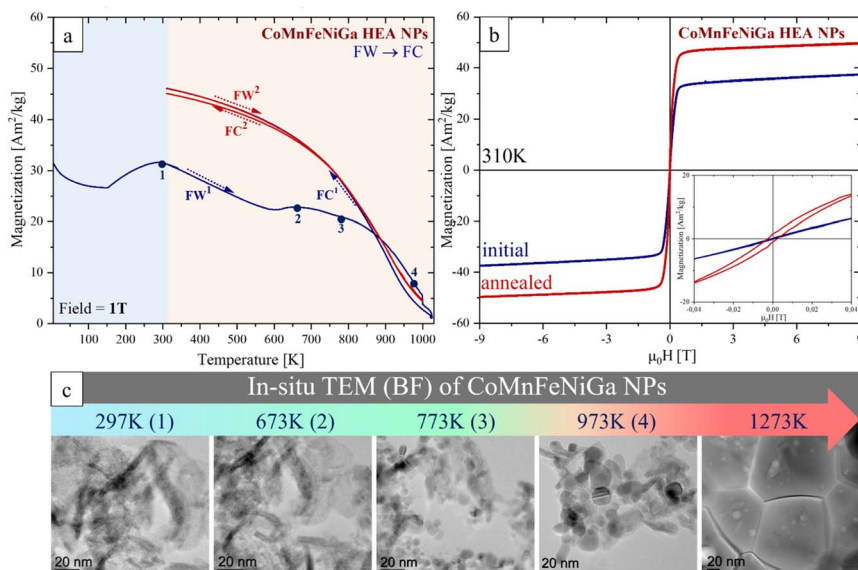
Fig. 10 CoMnFeNiGa HEA nanoparticles: (a) temperature-dependent magnetization (at 1 T in the temperature range 5–1000 K); (b) field-dependent magnetization at 310 K before and after annealing (−9 T ≥ B_{ext} ≥ 9 T); (c) BF-TEM images taken during *in situ* heating at different temperatures: 297 K, 673 K, 773 K, 973 K, 1273 K.

The $M(H)$ hysteresis loops measured at 310 K before and after annealing at 1000 K (30 s) (Fig. 10b) show a 40% enhanced M_s (310 K) = 46.9 A m^2 kg^{-1} and an increase of H_c by ∼3 times (up to 1.8 kA m^{-1}) compared to the initial state (M_s (310 K) = 33.5 A m^2 kg^{-1}; H_c = 0.6 kA m^{-1}) of the HEA NPs.

To understand the complex magnetic behavior of HEA NPs observed during annealing—most likely associated with thermally induced structural transitions—an *in situ* heating TEM experiment was conducted. Fig. 10c shows a set of BF-TEM images illustrating the microstructural evolution of CoMnFeNiGa HEA NPs during *in situ* heating at different temperatures: 297 K, 673 K, 773 K, 973 K, and 1273 K. Heating up to 673 K in TEM does not create significant differences in the NPs compared to the initial state (at 297 K). At T = 773 K the crystallization begins, while at 973 K, the grain growth accelerates followed by the phase transformation from 2D HEA hydroxide (birnessite-type layered δ-MnO$_2$ structure) to BCC and FCC phases. At 1273 K, the well-defined microstructure of large grains with small precipitates is formed (see details in S7 of the ESI†).

3.2.3 CoMnFeNiGa bulk. As demonstrated in Sections 3.2.1 and 3.2.2, the heat treatment of CoMnFeNiGa HEA micropowders and NPs up to 1000 K induces structural transformations: in the micropowder, an FCC → BCC phase transformation occurs, while in the NPs, the hexagonal structures (mainly, birnessite-type layered δ-MnO$_2$ structure) phase partially dissolves into a BCC + FCC mixture. In contrast, the SPS-consolidated HEA bulk, which already consists of a stable mixture of FCC and BCC phases, is not expected to undergo further structural changes upon heating to 1000 K—well below the SPS consolidation temperature of 1073 K. Consequently, no significant changes in its magnetic properties are
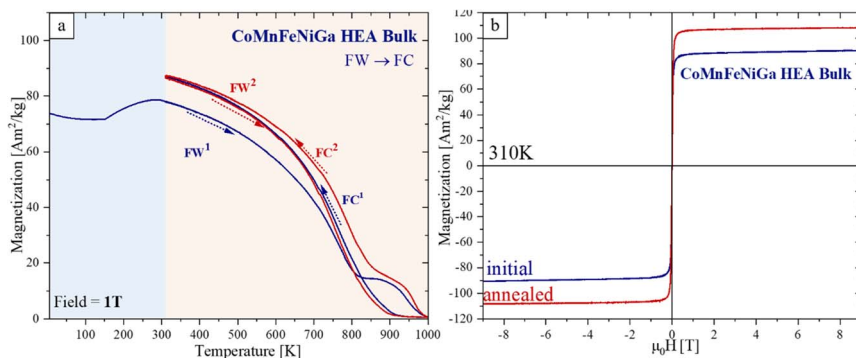
Fig. 11 CoMnFeNiGa HEA bulk: (a) temperature-dependent magnetization at 1 T in the temperature range (5–1000 K); (b) field-dependent magnetization at 310 K before and after annealing (-9 T $\geq B_{\text{ext}} \geq 9$ T).

anticipated. The experimental results, however, revealed slight deviations from this expectation.

The temperature-dependent magnetization $M(T)$ of the CoMnFeNiGa HEA bulk sample measured at $B_{\text{ext}} = 1$ T (Fig. 11a) shows an M (5 K) value of approximately 74 A m^2 kg^{-1} ($\sim$1.3 that of Ni). A similar magnetization behavior over the 5–290 K temperature range was also observed for the NPs, featuring an inflection point near $T = 150$ K. At this temperature, the M initially decreases, then increases again, reaching a maximum of 78.1 A m^2 kg^{-1}. Upon further heating, there is a gradual loss of magnetic order (FM $\rightarrow$ PM transition), with a complete disappearance of M at about 970 K. Notably, the FC^1 cycle (Fig. 11a, blue) results in an $\sim$12% increase in M, reaching 87.3 A m^2 kg^{-1} at 310 K. In addition, heat treatment leads to a 20% increase in M_{s} (310 K) = 106 A m^2 kg^{-1} (Fig. 11b, red), while the HEA bulk remains magnetically soft, with a low coercivity $H_{\text{c}} = 0$–0.5 kA m^{-1}.

The $T_{\text{c}} = 755$ K did not change before and after FW^1–FC^1, and it increased to 793 K after FC^2. We assume that this M and T_{c} enhancement is due to irreversible phase and local composition changes.

4. Discussion

4.1 Effect of processing route on phase formation, microstructure and composition in CoMnFeNiGa HEAs

Our study is a comprehensive investigation of CoMnFeNiGa HEAs synthesized through HEBM, SPS, and MP-LFL. Each processing route uniquely influences the resultant phase composition, microstructure, and chemical homogeneity across different length scales (powders, bulk, or NPs).

The successful formation of a single-phase FCC CoMnFeNiGa nanocrystalline structure ($\sim$8 nm) by short-term HEBM—despite the inclusion of low-melting Ga—demonstrates the advantages of this non-equilibrium approach. Furthermore, the morphology and microstructure of the HEA powder can be finely tuned by adjusting the milling conditions ("dry" or "dry + wet"), allowing control over particle shape, crystallite size, and microstrain.

Such phase purity and nanoscale compositional homogeneity (Fig. 2) were not achieved in previous studies, where Ga-containing HEAs synthesized *via* arc melting or casting typically resulted in multi-phase microstructures (*e.g.*, FCC + BCC mixtures or B2 ordering), often accompanied by significant phase segregation and the need for high temperature homogenization to reduce inhomogeneities.[19,21,23,24,26,28] Zuo *et al.*[24] reported that CoFeMnNiGa required extensive annealing to achieve phase uniformity, while Orbay *et al.*[26] observed that Ga additions led to structural separation and complex phase formation. In contrast, the HEBM creates a kinetically controlled environment that stabilizes the single-phase FCC structure and effectively suppresses segregation even in the presence of low-melting Ga.

SPS consolidation of HEA powders led to partial FCC → BCC transformation with nanoscale segregation into FeCo-rich (FCC) and NiGa-rich (BCC) regions which has not been previously reported in Ga-containing HEAs, where segregation is typically evident already at the microscale.[19,21,23,24,26,28] In addition, the formation of nanocrystalline (10–50 nm) Mn-rich BCC precipitates in both phases was observed (Fig. 6b), which may also influence magnetic domain behavior and local exchange interactions in the HEA bulk.

To the best of our knowledge, no previous studies have demonstrated the synthesis of HEA nanoparticles by MP-LFL, including CoMnFeNiGa. The LFL prepared NPs exhibited a complex multiphase structure dominated by a 2D high entropy layered hydroxide phase (birnessite-type layered δ-MnO_2 structure), along with minor residual FCC and BCC solid solution phases. Despite oxidation and phase segregation due to the metal–liquid interactions in the aqueous environment, the elemental mapping confirmed that the multi-elemental homogeneity was preserved across both spherical and platelet morphologies resulting from the fast cooling rates involved during NP formation.

4.2 Structure–magnetic properties correlations at different length scales in CoMnFeNiGa HEAs

The magnetic properties of CoMnFeNiGa HEAs are strongly influenced by phase composition, microstructural features, and morphology. The HEBM nanocrystalline single-phase FCC HEA powder (Fig. 8) exhibits a relatively weak FM response (M_s (310 K) = 19.5 A m^2 kg^{-1}, T_c = 240 K). This can be attributed to several factors: (a) the disordered FCC structure with high content of AFM Mn, which suppresses long-range FM exchange; (b) small crystallite size (∼8 nm) and HEBM-induced microstrain (∼0.4%) introduce additional structural disorder that may further hinder FM coupling and reduce M_s. This observation aligns with previous studies[18,41,42] showing that highly strained or fine-grained FCC HEAs tend to exhibit weak magnetic behavior unless partially transformed into BCC or chemically segregated phases. The higher H_c value observed in the HEA powder, relative to the NPs and bulk sample (Table 2), can be attributed to strain-induced lattice disorder, which hinders domain wall motion and enhances magnetic hardness.

In contrast, the SPS-consolidated bulk sample, containing a nanocrystalline dual-phase matrix (FeCo-rich FCC and NiGa-rich BCC regions), exhibits significantly improved magnetic properties (M_s = 88.8 A m^2 kg^{-1}, T_c = 764 K). This enhancement is attributed to the larger BCC phase fraction (∼87%), which favors

Table 2 Magnetic properties of CoMnFeNiGa HEAs before and after heat treatment (1000 K; 30 s)

HEA sample	M_s (5 K) [A m^2 kg^{-1}]	M_s (310 K) [A m^2 kg^{-1}]	H_c (5 K) [kA m^{-1}]	H_c (310 K) [kA m^{-1}]	T_c [K]
Non-annealed					
Powder	46.5	19.5	55	5.1	240
NPs	49.5	33.5	7.3	0.6	—
Bulk	96.2	88.8	2.2	0.5	764
Annealed at 1000 K (30 s)					
Powder	—	105.6	—	0.6	785
NPs	—	46.9	—	1.8	850
Bulk	—	106	—	0	755

stronger FM exchange interactions, as well as crystallite size growth (∼115–138 nm) and reduced microstrain, which improves domain alignment. The low H_c in the HEA bulk (3.6 kA m^{-1}) reflects the soft magnetic character of the dual-phase matrix and the lack of significant anisotropy or domain wall pinning, despite the presence of Mn-rich precipitates.

The HEA NPs, despite their structural complexity and the presence of a dominant 2D high-entropy layered hydroxide phase (birnessite-type δ-MnO$_2$ structure), have a sizeable M_s (310 K) = 33.5 A m^2 kg^{-1}—approximately 1.7 times higher than that of the HEA powder and one-third that of the SPS bulk. This relatively high M_s is likely driven by residual FCC and BCC HEA domains and may be further enhanced by interfacial exchange interactions between metallic and oxidized regions, which promote partial spin alignment at the interfaces. The low coercivity, on the other hand, is attributed to the weakly magnetic nature of the hydroxide phases, reduced lattice strain, and limited magnetic coupling between metallic domains. Additionally, the small size and structural separation of magnetic regions may contribute to thermally assisted magnetization reversal, leading to magnetically soft behavior.

These results underscore that magnetic performance is not solely dictated by elemental composition but is critically dependent on processing-induced phase formation and nanoscale structural and microstructural control.

4.3 Effect of heat treatment on structure and magnetic properties

The rapid thermal treatment at 1000 K (30 s, B_{ext} = 1 T) significantly improved the magnetic properties of CoMnFeNiGa HEAs across all length scales. In powders, a complete FCC → BCC transformation (at T = 569–724 K) resulted in a sharp increase in M_s up to 105.6 A m^2 kg^{-1} and T_c to 785 K (Table 2). These values are comparable to the best-performing BCC-type bulk HEAs with Ga or Al additions.[24,26,28] For instance, Hariharan et al.[27] reported similar gains in Al-doped CoFeMnNi HEA bulk only after extended homogenization at 1323 K (50 h), whereas we achieved comparable results using a much shorter annealing time and a significantly lower temperature of 1000 K, with no observable compositional loss.

Nanoparticles also showed marked increases in M_s to 46.9 A m^2 kg^{-1} and in T_c to 850 K—among the highest reported for HEA nanostructures. We also observed

an increase in H_c by 3 times (up to 1.8 kA m^{-1}) after annealing, suggesting enhanced magnetic anisotropy.

Bulk HEAs, while thermally stable due to prior SPS processing, still benefit from short thermal treatment, with M_s increasing by 20% (Table 2). Notably, this improvement occurred despite the annealing temperature (1000 K) being lower than the SPS sintering temperature (1073 K), indicating that local structural rearrangements can still contribute to the overall magnetic response.

Our findings not only confirm the magnetic benefits of Ga in HEAs reported in earlier studies but also extend them to new morphologies and processing routes. In contrast to previous works focused primarily on arc-melted or cast samples, this study establishes a scalable approach for producing nanostructured MagHEAs with tunable properties.

5. Conclusion

This study demonstrates a scalable and unique processing strategy for tailoring the structure, microstructure and magnetic properties of CoMnFeNiGa HEAs across different length scales—micropowder, bulk, and NPs. The HEBM enables the incorporation of low-melting Ga into a stable, single-phase FCC nano-crystalline HEA matrix. Subsequent SPS induces partial FCC → BCC trans-formation and nanoscale compositional segregation, producing dual-phase HEA bulk with enhanced magnetic performance. MP-LFL emerges as a robust synthesis platform for producing compositionally complex NPs in a single step directly from the HEBM microparticles. Metal–liquid interactions critically determine the NP morphology (spheres and platelets) and subsequent phase structure, offering promising avenues for solvent-dependent phase control while retaining multi-elemental homogeneity. Despite structural complexity, all forms exhibit RT ferromagnetism, with magnetic behavior governed by processing-induced variations in phase composition, crystallite size, and microstrain. A rapid thermal treatment (30 s) at 1000 K led to significant improvements in magnetic properties across all forms, driven by phase transformations and microstructural modification. This study provides a new pathway to engineer soft ferromagnetic HEAs with tailored properties by controlling phase composition, crystallite size, nanoscale chemical segregation, and processing-induced micro-structure through synthesis and subsequent heat treatment.

Data availability

The data supporting this article have been included as part of the supplementary information.†

Author contributions

NFSh: conceptualization, methodology, investigation, validation, visualization, writing – original draft, writing – review & editing. TS: methodology, investigation, validation, writing – review & editing. VN: methodology, investigation, writing – review & editing. LMF: methodology, investigation, validation, writing – review & editing. EA: methodology, investigation, validation, writing – review & editing. IT: investigation, validation. MG: investigation, validation. BG: investigation, writing

– review & editing. SR: writing – review & editing. LML: writing – review & editing. SB: supervision, writing – review & editing. MF: supervision, writing – review & editing.

Conflicts of interest

There are no conflicts to declare.

Acknowledgements

References

1 B. Cantor, I. T. H. Chang, P. Knight and A. J. B. Vincent, *Mater. Sci. Eng., A*, 2004, **375–377**, 213–218, DOI: **10.1016/j.msea.2003.10.257**.

2 J.-W. Yeh, S.-K. Chen, S.-J. Lin, J.-Y. Gan, T.-S. Chin, T.-T. Shun, C.-H. Tsau and S.-Y. Chang, *Adv. Eng. Mater.*, 2004, **6**, 299–303, DOI: **10.1002/adem.200300567**.

3 L. Han, Z. Rao, I. R. Souza, F. Maccari, Y. Wei, G. Wu, A. Ahmadian, X. Zhou, O. Gutfleisch, D. Ponge, D. Raabe and Z. Li, *Adv. Mater.*, 2021, **33**, 2102139, DOI: **10.1002/adma.202102139**.

4 Y. Zhang, T. Zuo, Y. Cheng and P. K. Liaw, *Sci. Rep.*, 2013, **3**, 1455, DOI: **10.1038/srep01455**.

5 J. Y. Law and V. Franco, *APL Mater.*, 2021, **9**, 080702, DOI: **10.1063/5.0058388**.

6 S.-M. Na, P. K. Lambert and N. J. Jones, *AIP Adv.*, 2021, **11**, 015210, DOI: **10.1063/9.0000097**.

7 D. B. Miracle and O. N. Senkov, *Acta Mater.*, 2017, **122**, 448–511, DOI: **10.1016/j.actamat.2016.08.081**.

8 S. J. Sun, Y. Z. Tian, H. R. Lin, X. G. Dong, Y. H. Wang, Z. J. Zhang and Z. F. Zhang, *Mater. Des.*, 2017, **133**, 122–127, DOI: **10.1016/j.matdes.2017.07.054**.

9 Z. M. Li, K. G. Pradeep, Y. Deng, D. Raabe and C. C. Tasan, *Nature*, 2016, **534**, 227, DOI: **10.1038/nature17981**.

10 B. Gludovatz, A. Hohenwarter, D. Catoor, E. H. Chang, E. P. George and R. O. Ritchie, *Science*, 2014, **345**, 1153–1158, DOI: **10.1126/science.1254581**.

11 M. Klimova, D. Shaysultanov, A. Semenyuk, S. Zherebtsov, G. Salishchev and N. Stepanov, *J. Alloys Compd.*, 2020, **849**, 156633, DOI: **10.1016/j.jallcom.2020.156633**.

12 N. F. Shkodich, K. V. Kuskov, A. S. Sedegov, I. D. Kovalev, A. V. Panteleeva, Y. S. Vergunova, Y. B. Scheck, E. Panina, N. Stepanov, I. Serhiienko and D. Moskovskikh, *J. Alloys Compd.*, 2022, **893**, 162030, DOI: **10.1016/j.jallcom.2021.162030**.

13 P. Koželj, S. Vrtnik, A. Jelen, M. Krnel, D. Gačnik, G. Dražić, A. Meden, M. Wencka, D. Jezeršek, J. Leskovec, S. Maiti, W. Steurer and J. Dolinšek, *Adv. Eng. Mater.*, 2019, **21**, 1801055, DOI: **10.1002/adem.201801055**.

14 B. Cantor, *Fundamentals of Multicomponent High-Entropy Materials*, Oxford University Press, 2024, DOI: **10.1093/9780191986710.001.0001**.

15 E. P. George, D. Raabe and R. O. Ritchie, *Nat. Rev. Mater.*, 2019, **4**, 515–534, DOI: **10.1038/s41578-019-0121-4**.

16 L. Kong, B. Cheng, D. Wan and Y. Xue, *Front. Mater.*, 2023, **10**, 1135864, DOI: **10.3389/fmats.2023.1135864**.

17 N. F. Shkodich, T. Smoliarova, H. Ali, B. Eggert, Z. Rao, M. Spasova, I. Tarasov, H. Wende, K. Ollefs, B. Gault and M. Farle, *Acta Mater.*, 2025, **284**, 120569, DOI: **10.1016/j.actamat.2024.120569**.

18 A. Takeuchi, K. Amiya, T. Wada, K. Yubuta and W. Zhang, *JOM*, 2014, **66**, 1984–1992, DOI: **10.1007/s11837-014-1085-x**.

19 M. C. Gao, B. Zhang, S. M. Guo, J. W. Qiao and J. A. Hawk, *Metall. Mater. Trans. A*, 2016, **47**, 3322–3332, DOI: **10.1007/s11661-015-3091-1**.

20 L. Han, S. Zhu, Z. Rao, W. Chen, H. Zhang, B. Li and Z. Lu, *Nat. Rev. Mater.*, 2024, **9**, 846–865, DOI: **10.1038/s41578-024-00720-y**.

21 S. Guo and C. T. Liu, *Prog. Nat. Sci.:Mater. Int.*, 2011, **21**, 433–446, DOI: **10.1016/S1002-0071(12)60080-X**.

22 X. Feng, R. Zheng, Z. Wu, Y. Zhang, Z. Li, X. Tan and H. Xu, *J. Alloys Compd.*, 2021, **882**, 160640, DOI: **10.1016/j.jallcom.2021.160640**.

23 T. T. Zuo, R. B. Li, X. J. Ren and Y. Zhang, *J. Magn. Magn. Mater.*, 2014, **371**, 60–68, DOI: **10.1016/j.jmmm.2014.07.023**.

24 T. Zuo, M. C. Gao, L. Ouyang, X. Yang, Y. Cheng, R. Feng, S. Chen, P. K. Liaw, J. A. Hawk and Y. Zhang, *Acta Mater.*, 2017, **130**, 10–18, DOI: **10.1016/j.actamat.2017.03.013**.

25 P. Li, A. Wang and C. T. Liu, *Intermetallics*, 2017, **87**, 21–26, DOI: **10.1016/j.intermet.2017.04.007**.

26 Y. Orbay, Z. Rao, A. Çakır, T. Tavşanoğlu, M. Farle and M. Acet, *Acta Mater.*, 2023, **259**, 119240, DOI: **10.1016/j.actamat.2023.119240**.

27 V. S. Hariharan, A. Karati, T. Parida, *et al.*, *J. Mater. Sci.*, 2020, **55**, 17204–17217, DOI: **10.1007/s10853-020-05171-8**.

28 T. Zuo, M. Zhang, P. K. Liaw and Y. Zhang, *Intermetallics*, 2018, **100**, 1–8, DOI: **10.1016/j.intermet.2018.05.014**.

29 N. F. Shkodich, I. D. Kovalev, K. V. Kuskov, D. Yu. Kovalev, Y. S. Vergunova, Y. B. Scheck, S. G. Vadchenko, O. Politano, F. Baras and A. S. Rogachev, *J. Alloys Compd.*, 2022, **893**, 161839, DOI: **10.1016/j.jallcom.2021.161839**.

30 S. Varalakshmi, M. Kamaraj and B. S. Murty, *J. Alloys Compd.*, 2008, **460**, 253, DOI: **10.1016/j.jallcom.2007.05.104**.

31 V. Amendola, D. Amans, Y. Ishikawa, N. Koshizaki, S. Scirè, G. Compagnini, S. Reichenberger and S. Barcikowski, *Chem.–Eur. J.*, 2020, **26**, 9206, DOI: **10.1002/chem.202000686**.

32 M. Spellauge, M. Tack, R. Streubel, M. Miertz, K. S. Exner, S. Reichenberger, S. Barcikowski, H. P. Huber and A. R. Ziefuss, *Small*, 2023, **19**, 2206485, DOI: **10.1002/smll.202206485**.

33 M. Tack, M. Usama, N. Kazamer, K. S. Exner, M. Brodmann, S. Barcikowski and S. Reichenberger, *ACS Appl. Energy Mater.*, 2024, **7**, 4057–4067, DOI: **10.1021/acsaem.4c00342**.

34 A. R. Ziefuß, S. Reichenberger, C. Rehbock, I. Chakraborty, M. Gharib, W. J. Parak and S. Barcikowski, *J. Phys. Chem. C*, 2018, **122**, 22125–22136, DOI: **10.1021/acs.jpcc.8b04374**.

35 P. Cavaliere, *Spark Plasma Sintering of Materials: Advancesin Processing and Applications*, 2019, DOI: **10.1007/978-3-030-05327-7**.

36 L. Lutterotti, *MAUD Tutorial – Instrumental Broadening Determination*, University of Trento, 2006.

37 K. Thompson, D. Lawrence, D. J. Larson, J. D. Olson, T. F. Kelly and B. Gorman, *Ultramicroscopy*, 2007, **107**, 131–139, DOI: **10.1016/j.ultramic.2006.06.008**.

38 T. Fromme, S. Reichenberger, K. M. Tibbetts and S. Barcikowski, *Beilstein J. Nanotechnol.*, 2024, **15**, 638–663, DOI: **10.3762/bjnano.15.54**.

39 B. M. Hunter, J. D. Blakemore, M. Deimund, H. B. Gray, J. R. Winkler and A. M. Müller, *J. Am. Chem. Soc.*, 2014, **136**, 13118–13121, DOI: **10.1021/ja506087h**.

40 R. F. Egerton, *Physical Principles of Electron Microscopy*, Springer, New York, 2005, DOI: **10.1007/b136495**.

41 V. Chaudhary, R. Chaudhary, R. Banerjee and R. V. Ramanujan, *Mater. Today*, 2021, **49**, 231–252, DOI: **10.1016/j.mattod.2021.03.018**.

42 N. Shkodich, F. Staab, M. Spasova, K. V. Kuskov, K. Durst and M. Farle, *Materials*, 2022, **15**, 7214, DOI: **10.3390/ma15207214**.